CORA Cork Open Research Archive
Cartlann Taighde Oscailte Chorcaí

Title	Atomic layer deposited electron transport layers in efficient organometallic halide perovskite devices
Authors	McCarthy, Melissa M.;Walter, Arnaud;Moon, Soo-Jin;Noel, Nakita K.;O'Brien, Shane;Pemble, Martyn E.;Nicolay, Sylvain;Wenger, Bernard;Snaith, Henry J.;Povey, Ian M.
Publication date	2018-07-03
Original Citation	McCarthy, M. M., Walter, A., Moon, S.-J., Noel, N. K., O'Brien, S., Pemble, M. E., Nicolay, S., Wenger, B., Snaith, H. J. and Povey, I. M. (2018) 'Atomic Layer Deposited Electron Transport Layers in Efficient Organometallic Halide Perovskite Devices', MRS Advances, 3(51), pp. 3075-3084. doi: 10.1557/adv.2018.515
Type of publication	Article (peer-reviewed)
Link to publisher's version	10.1557/adv.2018.515
Rights	© Materials Research Society 2018. This article has been published in a revised form in MRS Advances, http://dx.doi.org/10.1557/adv.2018.515 This version is free to view and download for private research and study only. Not for re-distribution, re-sale or use in derivative works.
Download date	2024-04-20 08:41:40
Item downloaded from	https://hdl.handle.net/10468/7616

UCC
University College Cork, Ireland
Coláiste na hOllscoile Corcaigh

Atomic Layer Deposited Electron Transport Layers in Efficient Organometallic Halide Perovskite Devices

Melissa M. McCarthy[1, 4], Arnaud Walter[2], Soo-Jin Moon[2], Nakita K. Noel[3], Shane O'Brien[1], Martyn E. Pemble[1, 4], Sylvain Nicolay[2], Bernard Wenger[3], Henry J. Snaith[3], Ian M. Povey[1]

[1]Tyndall National Institute, University Cork College, Lee Maltings Complex, Cork, Ireland
[2]Centre Suisse d'Electronique et de Microtechnique (CSEM), PV-Center, Jaquet-Droz 1, 2002 Neuchâtel, Switzerland.
[3]Department of Physics, University of Oxford, Clarendon Laboratory, Parks Road, Oxford, UK.
[4]School of Chemistry, University College Cork, Cork, Ireland.

ABSTRACT

Amorphous TiO_2 and SnO_2 electron transport layers (ETLs) were deposited by low-temperature atomic layer deposition (ALD). Surface morphology and x-ray photoelectron spectroscopy (XPS) indicate uniform and pinhole free coverage of these ALD hole blocking layers. Both mesoporous and planar perovskite solar cells were fabricated based on these thin films with aperture areas of 1.04 cm^2 for TiO_2 and 0.09 cm^2 and 0.70 cm^2 for SnO_2. The resulting cell performance of 18.3 % power conversion efficiency (PCE) using planar SnO_2 on 0.09 cm^2 and 15.3 % PCE using mesoporous TiO_2 on 1.04 cm^2 active areas are discussed in conjunction with the significance of growth parameters and ETL composition.

INTRODUCTION

In recent years organic-inorganic halide perovskites have gained significant interest due to their high PCEs. These high efficiencies can be attributed to the perovskites' tunable optical bandgap [1-4] and long carrier diffusion length [5-7], while their low fabrication cost [8] facilitates accelerated research. The first reported PCE using an organic-inorganic halide perovskite came from Kojima et al. [9] in 2009. The reported PCE of 3.8 % was achieved in conjunction with a liquid electrolyte. Since then, the perovskite field has been extensively studied and efficiencies now reach over 22 % [10]. Despite these advances, long term stability and scalability have remained major challenges [1, 11-13]. The rapid increase in PCE has largely been facilitated by the use of active areas markedly smaller than 1 cm^2. Similar efficiencies need to be achieved on up-scaled devices to ensure the viability of this photovoltaic technology.

TiO_2 is the most commonly used ETL in perovskite solar cells (PSCs) to date. The ETLs used in PSCs not only transfer electrons within the cell, but also act as a hole blocking layer preventing charge carrier recombination between the electrode contact and the light harvesting perovskite layer [14]. This function is dependent on a pinhole free hole blocking

layer which becomes difficult to maintain when scaled. Other hole blocking layers include C_{60} [15], ZnO [16] and SnO_2 [17-20]. The conformality of ALD allows for the deposition of very thin blocking layers over large areas when compared to conventional techniques [21-23].

In this study we examined the characteristics of different compact TiO_2 and SnO_2 layers fabricated using ALD. Surface morphological and XPS characterization indicate the ALD films were all conformal and pinhole free, and thus expected to perform well as blocking layers. However when incorporated into perovskite solar cells the performance of the differing layers produced more complicated results. ALD TiO_2 was observed to perform best in a cell with a mesoporous scaffold rather than a planar cell, while SnO_2 displayed promising results when incorporated into a planar cell.

EXPERIMENTAL DETAIL

Deposition of ETLs was carried out on two commercial ALD reactors, a Cambridge NanoTech Fiji F200 and a Picosun R200© system. All metal oxides were deposited at 185 °C to meet the thermal restrictions of perovskite/silicon heterojunction tandem cells, one of the promising applications for PSCs [24]. The Cambridge NanoTech Fiji F200 was employed for the growth of TiO_2 using Titanium (IV) isopropoxide (TTIP) and H_2O or Ar/O_2 plasma in an argon carrier flow as the metal precursor and oxygen sources respectively, leading to a deposition rate of 0.2 Å per cycle. The Picosun R200© grew both TiO_2 and SnO_2 using a N_2 carrier flow. For TiO_2 tetrakis (diemthylamido) titanium (TDMAT) and H_2O or Ar/O_2 plasma were used as the Ti precursor and co-reactants. The growth rate per cycle at 185 °C for TDMAT was 0.5 Å. ALD-SnO_2 was deposited using tetrakis (diemthylamido) tin (TDMASn) and water as the Sn precursor and co-reactant. The growth rate per cycle at 185 °C for TDMASn was 0.6 Å. All metal precursors were purchased from STREM Chemicals Inc. Prior to being introduced into the ALD chamber, FTO/Glass substrates, (TEC-7, 7 Ω cm^{-1}) Solaronix, were cleaned by ultra-sonication in Decon 90, acetone, and IPA successively. FTO/Glass substrates, (TEC-7, 7 Ω cm^{-1}) Hartford Glass Co., were cleaned with 2% Hellmanex, deionized water, acetone, methanol and treated under oxygen plasma for 10 min successively. Where indicated samples were subjected to a 5 min O_2 plasma treatment in situ in the ALD chamber at a plasma power of 300 W prior to or following deposition.

For mesoporous cells, the mesoporous TiO_2 (m-TiO_2) layer (Sharechem) in isopropanol (1:5 dilution) was spin coated onto the ALD TiO_2 blocking layer coated FTO substrates (Solaronix) at 4500 rpm for 30 s to form a scaffold layer. The samples were dried at 125 °C and then sintered at 500 °C for 15 min. Both mesoporous and planar TiO_2 samples used the same perovskite recipe for $CH_3NH_3PbI_3$. FTO/TiO_2 substrates were exposed to 15 min O_3 prior to perovskite deposition for planar cells. A 1.4 M solution of PbI_2 (TCI) and CH_3NH_3I (Dyesol) in DMSO:DMF (Sigma Aldrich) was spin coated on substrates at 1000 rpm for 10 s, followed by 5000 rpm for 45 s. Diethyl ether (Sigma Aldrich) was used as an anti-solvent treatment 35 s before the end of the spin coating process. Substrates were then dried for 2 min at 50 °C and annealed for 10 min at 100 °C. The hole transport layer (HTL) was prepared by dissolving 72.3 mg 2,2',7,7'-tetrakis-(N,N-di-4-methoxyphenylamino) -9,9'spirobi-fluorenes (Spiro-OMeTAD) (Merck) in 28.8 µl/ml 4-tert-butylpyridine (tBP) (TCI), 17.5 µl/ml stock solution of 520 mg/ml lithium bis (trifluoromethylsulfonyl) imide (Li-TFSI) (Sigma-Aldrich) in acetonitrile, in 1 ml chlorobenzene. This was spin coated on top of the perovskite layer at 4000 rpm for 30 s. The devices were completed with the evaporation of a 100 nm gold electrode.

For devices where ALD-SnO_2 was used as an ETL in planar perovskite cells C_{60} was deposited as a buffer layer and the perovskite was processed through an ACN/CH_3NH_2 deposition route as described by Noel et al. [25]. In this process the HTL was prepared by dissolving Spiro-OMeTAD in chlorobenzene with additives at a concentration of 30 mM Li-TFSI and 80 mM tBP. The solar cell was completed with the evaporation of a 110 nm silver electrode.

CHARACTERIZATION

Dark conductivity measurements of the TiO_2 samples were performed under a 1 mbar N_2 atmosphere. During the measurement, the temperature was ramped from room temperature to 180 °C at a rate of 10 °C min^{-1}. The sample was then cooled at a rate of 1 °C min^{-1}. The conductivity was measured during the cooling phase. XRD was performed using a Philips X'pert PM3719 powder x-ray diffractometer with Cu Kα radiation (λ = 1.540598 Å). The morphologies of the deposited ALD films were examined using scanning electron microscopy (SEM, FEI Quanta FEG 650). Contact angle was performed at room temperature using a Dataphysics OCA 20 wetting angle system. Optical measurements (UV-Vis-NIR) were performed with a Perkin-Elmer Lambda 900 spectrophotometer. Elemental composition was determined by x-ray photoelectron spectroscopy (XPS) using a Kratos AXIS_ULTRA with a monochromatized Al Kα x-ray excitation source (10 mA, 15 kV) at 1486.58 eV). All XPS samples underwent a light etch using a monochromatic Ar beam (500 eV, 0.36 kV) for 10-15 seconds to remove the surface carbon layers before measurement. I-V measurements were carried out using a Cascade Microtech (Summit™ 12971 B-S) AttoGuard® probe station.

Perovskite cells with TiO_2 ETLs were measured under a two-lamp class AAA WACOM sun simulator with an AM 1.5 G irradiance spectrum at 100 W cm^{-2}. The cell area was defined using a metal mask. The J–V characteristics of the cells were obtained under both reverse (from Voc to Jsc) and forward (from Jsc to Voc) bias. A maximum power point (MPP) tracking was usually performed to extract the stabilized power output. External quantum efficiency (EQE) spectra were acquired on a custom-made spectral response setup equipped with a xenon lamp, a grating monochromator and lock-in amplifiers [26].

Perovskite cells with SnO_2 ETLs were measured using a class AAB ABET solar simulator with an AM 1.5 G irradiance spectrum at 100 mW cm^{-2}. The irradiance was calibrated using an NREL-calibrated KG5 filtered silicon reference cell. The J-V characteristics of the cell were recorded using a sourcemeter (Keithley 2400, USA). The cell areas were defined using a metal mask [25].

RESULTS AND DISCUSSION

Arrhenius plots of the surface conductivity of ALD TiO_2 thin films on glass are illustrated in Figure 1, demonstrating semi-conducting behavior for all films with conductivity increasing as temperature increases. In addition, it can be seen that the bulk conductivity of the thin films is precursor dependent. The titanium precursor, TTIP, was found to be a less reactive precursor at the low deposition temperature of 185 °C, requiring O_2 plasma as a co-reactant to achieve a growth rate of 0.2 Å per cycle. The titanium precursor, TDMAT, was found to be more reactive, requiring only H_2O as a co-reactant to produce a higher growth rate of 0.5 Å per cycle at 185 °C. The higher reactivity of TDMAT also allows for better coverage, approaching ideal monolayer growth, resulting in a more uniform microstructure. It is

expected that this better coverage is the reason for improved electrical properties [27]. It is of significance that samples subjected to a 5 min O_2 plasma treatment prior to being deposited using TDMAT and H_2O demonstrate a marked improvement in conductivity over all other methods of depositing TiO_2 by ALD. The plasma clean immediately preceding deposition is likely to provide more nucleation sites for the TDMAT reaction through an increased density of surface OH species and the removal of adventitious carbon species [28]. From this data it was decided that all TiO_2 depositions in this study would use TDMAT and H_2O as a precursor and co-reagent, respectively.

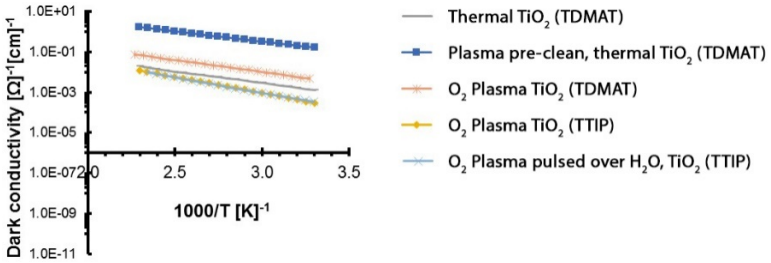

Figure 1: Arrhenius plot of the surface conductivity of ALD TiO_2 thin films demonstrating the importance of precursors and pre growth surface treatments.

As would be expected at a deposition temperature of 185 °C, all ALD films in this study were found to be amorphous as grown. Plan view SEM, Figure 2b, confirms the conformality with the morphology of the film matching that of a blank FTO substrate (not shown). Optical transmittance on quartz, Figure 2a, was found to scale with thickness, with values above 65 % being retained in the 400 nm – 1400 nm range of the spectrum even in the thickest film. XPS of a 20 nm TiO_2 film pre-treated with O_2 plasma allowed an estimate of the stoichiometry from the peak areas (Ti 2p peaks at 457.3 and 458.9 eV) to give a Ti^{3+}/Ti^{4+} ratio of 0.255:1. In general, the existence of Ti^{3+} in TiO_2 indicates that oxygen vacancies are generated to maintain an electrostatic balance. No signal was detected from the underlying FTO supporting the claim of conformal and pinhole free coverage. Contact angle measurements were carried out on the ETL to determine how well the perovskite layer would wet the surface when spin-coated. The measured contact angle of 76.1 °, using 1 µl water, indicates good wetting.

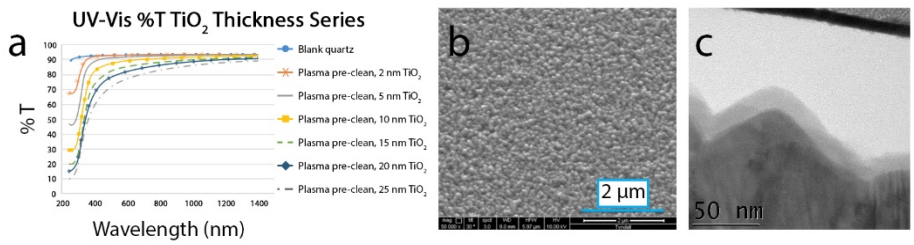

Figure 2: (a) % Transmission spectra **(b)** Plan view SEM showing surface morphology **(c)** TEM of 20 nm ALD-TiO_2 pre-treated with O_2 plasma.

20 nm TiO_2 was chosen to be fabricated as the compact hole blocking layer in a mesoporous perovskite solar cell. Despite the belief that ALD could enable a thinner blocking layer, a thickness of 20 nm TiO_2 was chosen to allow comparison with equivalent thicknesses from other viable ETL deposition processes used in our laboratories. Furthermore, it was believed that thinner amorphous ALD films would not be able to stand the high temperature anneal (500 °C) employed in the mesoporous perovskite solar cell fabrication without cracking and hence forming shunt pathways. The solar cell devices were composed of a conductive FTO coated glass substrate, a compact 20 nm ALD-TiO_2 thin film, a mesoporous TiO_2 layer, a $CH_3NH_3PbI_3$ perovskite layer, a Spiro-OMeTAD hole transport layer and a gold counter electrode. A batch of four devices was fabricated per ALD-TiO_2 variable, with the best performing of each sample set presented here. Three device sets with different 20 nm TiO_2 ETLs were fabricated alongside each other to avoid variations in the other layers mentioned above. Device 1 consisted of a 20 nm ALD-TiO_2 ETL without a plasma treatment. The ETL for device 2 employed 20 nm ALD-TiO_2 pre-treated with a 5 min O_2 plasma clean. Device 3 incorporated a 20 nm ALD-TiO_2 ETL with a 5 min O_2 plasma treatment post deposition. Table I summarizes the J-V cell results for the different ETL perovskite solar cell systems along with MPP tracking over 300 s. The J-V characteristics of the best PSC based on ALD-TiO_2 is shown in Figure 3a and the corresponding external quantum efficiency is displayed in Figure 3b. Device 2 containing a plasma pre-clean, 20 nm ALD-TiO_2 compact layer had a Voc, Jsc, and FF of 1097 mV, 19.80 mA cm^{-2}, and 70.61 %, respectively, leading to a PCE of 15.33 %. EQE displayed a current density of 12.26 mA cm^{-2} without a light bias, which is not in agreement with J-V results. When a white light bias is applied the current density reaches 16.54 mA cm^{-2} which is still below the value predicted by J-V. There is a clear photo-doping effect observed in the ALD layer. This effect was exhibited in all ALD samples except that which was given an O_2 plasma treatment *after* ALD deposition. It is speculated that the O_2 plasma treatment after ALD growth allowed the formation of an improved interface between the blocking c-TiO_2 and the m-TiO_2 by removing defects and charge traps, and consequently improving wettability and thus the macroscopic features in fabrication [29]. While this procedure has not yet been fully optimized as indicated by the low efficiency of device 3, the removal of the observed photo-doping effect is significant.

Table I: Summary of IV parameters for different compositions of 20 nm TiO_2 ETLs in mesoporous perovskite solar cells. Device 1: 20 nm TiO_2 ALD. Device 2: 5 min O_2 plasma treatment followed by 20 nm TiO_2 ALD. Device 3: 20 nm TiO_2 ALD followed by 5 min O_2 plasma treatment.

Device #	Aperture area (cm^2)	Scan direction	Voc (mV)	Jsc (mA/cm^2)	FF (%)	Eff (%)	Steady-state MPP over 300 s (%)
1	1.04	Reverse	1091	20.056	64.135	14.422	13.7
		Forward	1100	19.583	59.360	13.405	
2	1.04	Reverse	1097	19.797	70.614	15.330	14.3

		Forward	1088	19.541	68.784	14.621	
3	1.04	Reverse	1069	18.851	58.744	11.841	8.5
		Forward	1062	18.300	60.090	11.680	

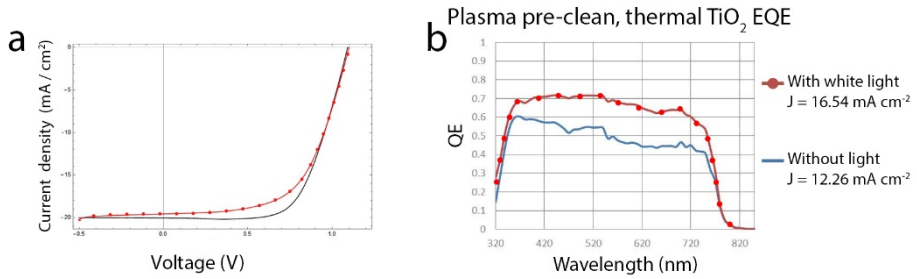

Figure 3: (a) J–V characteristics of mesoporous perovskite solar cell containing plasma clean, 20 nm TiO_2. **(b)** External quantum efficiency of same perovskite solar cell containing plasma pre-clean, 20 nm TiO_2 ETL.

The ETL in the best performing mesoporous perovskite device was then utilized in a planar perovskite cell. This cell consisted of a conductive FTO coated glass substrate, a compact 20 nm ALD-TiO_2 thin film, a $CH_3NH_3PbI_3$ perovskite layer, a Spiro-OMeTAD hole transport layer and a gold counter electrode. The mesoporous TiO_2 layer contained in mesoporous PSCs requires annealing at 500 °C. This high temperature anneal was shown to increase the resistance characteristics in the ALD-TiO_2 layer by several orders of magnitude. Removal of the mesoporous layer could allow for higher efficiency in the overall cell containing ALD-TiO_2. Planar PSCs are useful for adaptation into tandem cells which consist of a perovskite solar top-cell over a low bandgap bottom-cell (Si or CdTe, or CIGS or low bandgap perovskite). This would allow efficient light absorption over a much wider wavelength range. Perovskite cells for use in tandem solar cells would require an all-low temperature process to avoid degrading temperature sensitive layers (<200 °C). However the planar cell behaved much less effectively than the mesoporous cell employing the same ETL of 20 nm TiO_2 pre-treated with 5 min O_2 plasma clean. A max PCE of 8% was achieved with a significantly lower current and fill factor than previously observed. Although annealing the mesoporous cells at 500 °C increases the resistivity of the ALD TiO_2 films, it was determined by examination of the XPS of the Ti 2p signatures that the stoichiometry was improved by the anneal as the ratio of Ti^{3+} to Ti^{4+} was reduced from 1:3.9 to 1:4.3. As deposited TiO_2 from the TDMAT ALD process at 185 °C was found, in addition to being non-stoichiometric, to contain measurable quantities of N and C from unreacted precursors. The highly defective nature of the as grown material could give rise to significant charge trapping in both the bulk and the interface. Interface passivation is one avenue that could be explored to improve the performance of ALD-TiO_2 in planar cells. Another option would be to employ rapid thermal annealing to attempt to improve the quality of the ETL. However the increased thermal budget of this latter method would make it unlikely to be suitable for use in tandem cells.

Although TiO_2 is frequently used as an ETL in PSCs, it does come with some substantial disadvantages. Planar perovskite solar cells which employ TiO_2 are restricted due to a

conduction band misalignment with the perovskite layer. These types of solar cells exhibit unstable PCEs as electron injection is energetically hindered by the mismatched bands. As a result, accumulation of photogenerated charges can occur which can hamper the performance of the devices. TiO_2 also provides poor charge extraction which gives pronounced hysteresis in current-voltage curves. One alternative option to TiO_2 is SnO_2. Its deep conduction band enables a barrier-free band alignment between the perovskite light-harvester and the ETL.

The optical transmittance spectra of SnO_2 are shown in Figure 4a. As with the TiO_2, a general decrease in transmission can be observed as the films increase in thickness from 2 nm to 25 nm. Values above 75 % were retained even in the case of the thickest film in the 400 nm – 1400 nm range of the spectrum. A plan view SEM image of the SnO_2 thin film at 20 nm deposited on a FTO coated glass substrate is presented in Figure 4b and a cross-sectional TEM of a 10 nm SnO_2 film deposited on a FTO coated glass substrate can be seen in Figure 4c. The morphology of the thin film again matched the blank FTO. The Sn XPS of the ALD SnO_2 films (not shown) confirm stoichiometric SnO_2. Additionally as no signal was detected from the underlying FTO it is proposed that the coverage is pinhole free. The measured contact angle of 121.9 °, using 1 µl of water, indicates poor wetting. Thus an O_3 or O_2 plasma treatment before deposition of the perovskite is required for this metal oxide to be fabricated into a planar PSC. Contact angle measurements performed after 15 minutes of O_2 plasma treatment demonstrate a reduction from 121.9 ° to 3.8 °, indicating a super hydrophilic surface.

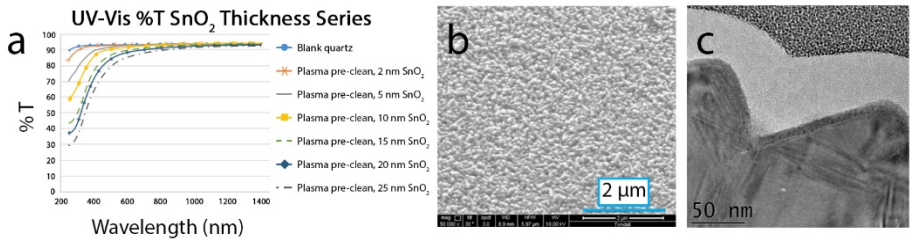

Figure 4: (a) % Transmission spectra (**b)** Plan view SEM showing surface morphology of 20 nm ALD-SnO_2 pre-treated with O_2 plasma **(c)** TEM of 10 nm ALD-SnO_2 pre-treated with O_2 plasma.

Electrical comparisons between 20 nm films pre-treated with O_2 plasma on a pad size of 200 µm reveal that SnO_2 exhibits an improvement in resistivity over TiO_2, as observed in Figure 5a. This indicates that SnO_2 may behave more effectively in a solar cell. In an attempt to further improve the fill factor a 10 nm ALD ETL with an O_2 plasma pre-clean was chosen for the SnO_2 planar perovskite solar cell. The solar cell devices were composed of a conductive FTO coated glass substrate (TEC-7, 7 Ω cm^{-1} Hartford Glass Co.), an ALD-SnO_2 thin film, a $CH_3NH_3PbI_3$ perovskite layer, a Spiro-OMeTAD hole transport layer, and a silver counter electrode. A batch of six devices containing ALD-SnO_2 was investigated with the best performing for each active area presented here. The performance of ALD SnO_2 in the planar architecture is summarized in Table II for two cell areas, 0.09 cm^2 and 0.7 cm^2. For a SnO_2 ETL in a planar configuration the current and fill factor were significantly improved compared to the planar architecture cells which incorporated TiO_2, although it is noted that the active area was reduced. J-V characteristics along with MPP tracking of these cells are shown in Figure

5b. The 0.09 cm^2 device exhibited a Voc, Jsc, and FF of 1070 mV, 23 mA cm^{-2}, and 75%, respectively, culminating in a PCE of 18.3 %.

The thermal ALD SnO_2 method is comparable to alternative low-temperature SnO_2 processes reported in the literature and shows the capacity for further optimization of this material system. Ke et al. achieved 17.21 % efficiency on a 0.09 cm^2 active area by spin-coating a solution of $SnCl_2{\cdot}2H_2O$ and annealing to 180 °C [30]. Jiang et al. employed a SnO_2 particle solution processed at 150 °C as an ETL incorporating a PbI_2 passivation phase in the perovskite layer. These cells reached a certified high PCE of 19.9 % and were almost hysteresis free on an active area of 0.108 cm^2 [31]. Plasma-Enhanced ALD (PEALD) has also been utilized to deposit SnO_2 as in the case of Wang et al. [32]. PEALD SnO_2 deposited at 100 °C produced an average PCE of 18.21 % on an active area of 0.08 cm^2 with the incorporation of a C_{60} passivating self-assembled monolayer.

The use of thermal ALD in this paper shows considerable promise for further development on up-scaling the active area, as well as the potential to be incorporated into a *p-i-n* architecture without damage to the perovskite under layer.

Table II: Device performance parameters for an ETL of 10 nm ALD-SnO_2 pre-treated with a 5 min O_2 plasma clean

Aperture area (cm^2)	Voc (mV)	Jsc (mA/cm^2)	FF (%)	Eff (%)	Steady-state MPP (%)
0.7	1070	22.5	67	15.8	15.8
0.09	1070	23.0	75	18.3	17.9

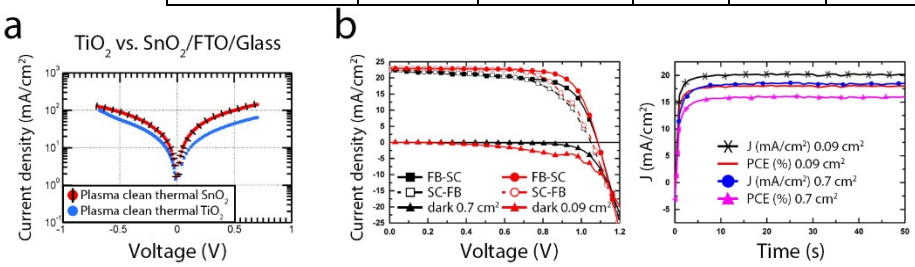

Figure 5 (a) I-V comparing conductivity of 20 nm ALD-TiO_2 pre-treated with 5 min O_2 plasma to 20 nm ALD-SnO_2 pre-treated with a 5 min O_2 plasma **(b)** I–V characteristics of planar perovskite solar cells containing 10 nm ALD-SnO_2 pre-treated with 5 min O_2 plasma.

CONCLUSIONS

In this study both TiO_2 and SnO_2 were deposited by low-temperature ALD and incorporated into perovskite solar cells using the precursors TDMAT and TDMASn, respectively. A 5 min O_2 plasma treatment prior to the amorphous deposition of thin films was found to improve PCE. Cells containing 20 nm TiO_2 achieved a PCE of 15.3 % on a 1.04 cm^2 area in a mesoporous architecture but failed to work as effectively in a planar structure. Further study is required to determine if this is due to an issue with interface passivation or bulk TiO_2. Cells containing 10 nm SnO_2 exhibited promising results achieving 18.3 % PCE on a 0.09 cm^2 area and 15.8 % PCE on a 0.70 cm^2 area in planar cells. Studies are ongoing to improve cell performance and investigate cell stability.

ACKNOWLEDGMENTS

This work is part of the CHEOPS project, which has received funding from the European Union's Horizon 2020 research and innovation program under grant agreement No. 653296.

REFERENCES

1. J. H. Noh, S. H. Im, J. H. Heo, T. N. Mandal, and S. I. Seok, Nano Lett., **13** (4), 1764-1769 (2013).
2. Y. Ogomi, A. Morita, S. Tsukamoto, T. Saitho, N. Fujikawa, Q. Shen, T. Toyoda, K. Yoshino, S. S. Pandey, T. Ma, and S. Hayase, J. Phys. Chem. Lett., **5** (6), 1004-1011 (2014).
3. G. E. Eperon, S. D. Stranks, C. Menelaou, M. B. Johnston, L. M. Herza, and H. J. Snaith, Energy Environ. Sci., **7**, 982-988 (2014).
4. J. Berry, T. Buonassisi, D. A. Egger, G. Hodes, L. Kronik, Y.-L. Loo, I. Lubomirsky, S. R. Marder, Y. Mastai, J. S. Miller, D. B. Mitzi, Y. Paz, A. M. Rappe, I. Riess, B. Rybtchinski, O. Stafsudd, V. Stevanovic, M. F. Toney, D. Zitoun, A. Kahn, D. Ginley, and D. Cahen, Adv. Mater., **27**, 5102-5112 (2015).
5. G. Xing, N. Mathews, S, Sun, S. S. Lim, Y. M. Lam, M. Grätzel, S. Mhaisalkar, and T. C. Sum, Science, **342** (6156), 344-347 (2013).
6. S. D. Stranks, G. E. Eperon, G. Grancini, C. Menelaou, M. J. P. Alcocer, T. Leijtens, L. M. Herz, A. Petrozza, and H. J. Snaith, Science, **342** (6156), 341-344 (2013).
7. Q. Dong, Y. Fang, Y. Shao, P. Mulligan, J. Qiu, L. Cao, and J. Huang, Science, **347** (6225), 967-970 (2015).
8. D. B., Mitzi, K. Chondroudis, and C. R. Kagan, IBM J. Res. DeV., **45** (1), 29-45 (2001).
9. A. Kojima, K. Teshima, Y. Shirai, and T. Miyasaka, J. Amer. Chem. Soc., **131** (17), 6050-6051 (2009).
10. National Renewable Energy Laboratory: Efficiency Chart (2018). Available at: https://www.nrel.gov/pv/assets/images/efficiency-chart.png (accessed 14 March 2018).
11. P. Pistor, J. Borchert, W. Fränzel, R. Csuk, and R. Scheer, J. Phys. Chem. Lett., **5** (19), 3308-3312 (2014).
12. S. Ito, S. Tanaka, K. Manabe, and H. Nishino, J. Phys. Chem. C, **118** (30), 16995-17000 (2014).
13. J.-P. Correa-Baena, M. Saliba, T. Buonassisi1, M. Grätzel, A. Abate, W. Tress, and A. Hagfeldt, Science, **358** (6364), 739-744 (2017).
14. H.-H. Wang, Q. Chen, H. Zhou, L. Song, Z. St Louis, N. De Marco, Y. Fang, P. Sun, T.-B. Song, H. Chena, and Y. Yang, J. Mater. Chem. A, **3**, 9108-9115 (2015).
15. K. Wojciechowski, T. Leijtens, S. Siprova, C. Schlueter, M. T. Hörantner, J. T. Wang, C.-Z. Li, A. K.-Y. Jen, T.-L. Lee, and H. J. Snaith, J. Phys. Chem. Lett. **6** (12), 2399-2405 (2015).
16. D. Liu and T. L. Kelly, Nat. Photonics, **8**, 133-138 (2014).
17. W. Ke, G. Fang, Q. Liu, L. Xiong, P. Qin, H. Tao, J. Wang, H. Lei, B. Li, J. Wan, G. Yang, and Y. Yan, J. Am. Chem. Soc., **137**, 6730-6733 (2015).

18. Y. Li, J. Zhu, Y. Huang, F. Liu, M. Lv, S. Chen, L. Hu, J. Tang, J. Yaod, and S. Dai, RSC Adv., **5**, 28424-28429 (2015).
19. Q. Dong, Y. Shi, K. Wang, Y. Li, S. Wang, H. Zhang, Y. Xing, Y. Du, X. Bai, and T. Ma, J. Phys. Chem. C., **119** (19), 10212-10217 (2015).
20. J.-P. Correa Baena, L. Steier, W. Tress, M. Saliba, S. Neutzner, T. Matsui, F. Giordano, T. J. Jacobsson, A. R. Srimath Kandada, S. M. Zakeeruddin, A. Petrozza, A. Abate, M. Khaja Nazeeruddin, M. Grätzel, and A. Hagfeldt, Energy Environ. Sci., **8**, 2928-2934 (2015).
21. L. Kavan, L. Steier, and M. Grätzel, J. Phys. Chem. C., **121** (1), 342-350 (2017).
22. Y. Wu, X. Yang, H. Chen, K. Zhang, C. Qin, J. Liu, W. Peng, A. Islam, E. Bi, F. Ye, M. Yin, P. Zhang, and L. Han, Appl. Phys. Express, **7**, 052301 (2014).
23. H. M. Yates, M. Afzaal, A. Walter, J. L. Hodgkinson, S-J. Moon, D. Sacchetto, M. Bräuninger, B. Niesen, S. Nicolay, M. M. McCarthy, M. E. Pemble, I. M. Povey, and C. Ballif, J. Mater. Chem. C, **4**, 11269-11277 (2016).
24. J. P. Mailoa, C. D. Bailie, E. C. Johlin, E. T. Hoke, A. J. Akey, W. H. Nguyen, M. D. McGehee, and T. Buonassisi, Appl. Phys. Lett. **106**, 121105 (2015).
25. N. K. Noel, S. N. Habisreutinger, B. Wenger, M. T. Klug, M. T. Hörantner, M. B. Johnston, R. J. Nicholas, D. T. Moore, and H. J. Snaith, Energy Environ. Sci., **10**, 145-152 (2017).
26. A. Walter, S-J. Moon, B. A. Kamino, L. Lofgren, D. Sacchetto, F. Matteocci, B. Taheri, J. Bailat, A. Di Carlo, C. Ballif, and S. Nicolay, IEEE J. Photovolt., **8** (1), 151-155 (2018).
27. Q. Xie, Y.L. Jiang, C. Detavenier, D. Deduytsche, R.L. Van Meirhaeghe, G.P. Ru, J. Appl. Phys., **102**, 083521 (2007).
28. K. Choi, S. Ghosh, J. Lim, C.M. Lee, Appl. Surfaces Science, **206**, 355-364 (2003).
29. M.R. Sanchis, V. Blanes, M. Blanes, D. Garcia, R. Balart, European Polymer Journal, **42**, 1558–1568 (2006).
30. W. Ke, G. Fang, Q. Liu, L. Xiong, P. Qin, H. Tao, J. Wang, H. Lei, B. Li, J. Wan, G. Yang, Y. Yan, J. Am. Chem. Soc., **137**, 6730–6733 (2015)
31. Q. Jiang, L. Zhang, H. Wang, X. Yang, J. Meng, H. Liu, Z. Yin, J. Wu, X. Zhang, J. You, Nat. Energy, **2**, 16177 (2016).
32. C. Wang, D. Zhao, C. Grice, W. Liao, Y. Yu, A. Cimaroli, N. Shrestha, P. J. Roland, J. Chen, Z. Yu, P. Liu, N. Cheng, R. Ellingson, X. Zhao and Y. Yan, J. Mater. Chem. A, **4**, 12080–12087 (2016).

At the date this manuscript was written, URLs or links referenced herein were deemed to be useful supplementary material to this manuscript. Neither the author nor the Materials Research Society warrants or assumes liability for the content or availability of URLs referenced in this manuscript.